Magnetohydrodynamic control of differential rotation and dynamo transitions: Rise of the local magnetic Rossby number

Krista M. Soderlund,[1]★ Paula Wulff[2], Petri J. Käpylä,[3], and Jonathan M. Aurnou[2]
[1]Institute for Geophysics, Jackson School of Geosciences, The University of Texas at Austin, USA
[2]Department of Earth, Planetary, and Space Sciences, University of California, Los Angeles, USA
[3]Institute for Solar Physics (KIS), Georges-Köhler-Allee 401a, Freiburg, 79110, Germany

Accepted XXX. Received YYY; in original form ZZZ

ABSTRACT

We investigate how the strength of the Lorentz force alters stellar convection zone dynamics in a suite of buoyancy-dominated, three-dimensional, spherical shell convective dynamo models. This is done by varying only the fluid's electrical conductivity via the non-dimensional magnetic Prandtl number, *Pm*. Because the strength of the dynamo magnetic field and the Lorentz force scale with *Pm*, it is found that the fluid motions and mode of dynamo generation differ across the $0.25 \leq Pm \leq 10$ range investigated here. For example, we show that strong magnetohydrodynamic effects cause a fundamental change in the surface zonal flows: differential rotation switches from solar-like with prograde equatorial zonal flow for larger electrical conductivities (i.e., stronger dynamo magnetic field) to an anti-solar differential rotation with retrograde equatorial zonal flow at lower electrical conductivities (i.e., weaker magnetic field). This study shows that the value of electrical conductivity is important not only for sustaining dynamo action, but can also drive first-order changes in the characteristics of the magnetic and velocity fields. It is further associated with the ratio of inertial and Lorentz forces, estimated by the local magnetic Rossby number, $Ro_{M,\ell}$. We show in our models that $Ro_{M,\ell}$ sets the characteristics of the large-scale convection regime that generates the dynamo fields, with $Ro_{M,\ell} \lesssim 1$ (Lorentz dominated) corresponding to solar-like differential rotation and $Ro_{M,\ell} \gtrsim 1$ (inertia dominated) corresponding to anti-solar-like differential rotation.

Key words: convection – dynamo – Sun: interior – Sun: magnetic fields – Sun: rotation

1 INTRODUCTION

The dynamics of stellar convection zones are dominated by nonlinear interactions between large-scale differential azimuthal flows and meridional overturning circulations, which together drive the generation of stellar-scale magnetic fields (e.g., Miesch & Toomre 2009; Käpylä et al. 2023). The interplay of turbulent convection and large-scale circulations also acts to drive latitudinal gradients in surface luminosity, which can act back on the differential rotation (DR) (e.g. Aurnou et al. 2008; Soderlund et al. 2013; Käpylä et al. 2020). Such complex systems can have multiple behavioral regimes (e.g Viviani et al. 2019; Hindman et al. 2020; Menu et al. 2020; Camisassa & Featherstone 2022; Zaire et al. 2022). Defining these regimes and elucidating their essential physics are necessary to understand the behavior of our sun and stars in general (e.g. Reinhold & Arlt 2015; Metcalfe et al. 2016; Lehtinen et al. 2021).

It has been posited in numerous studies that stellar differential rotation is primarily controlled by rotational hydrodynamics in the convection zone (e.g., Gilman 1977, 1978; Gilman & Foukal 1979; Glatzmaier & Gilman 1981; Gastine et al. 2013; Gastine et al. 2014b; Guerrero et al. 2013; Käpylä et al. 2014; Mabuchi et al. 2015; Viviani et al. 2018; Camisassa & Featherstone 2022). This hydrodynamic control is parameterized via the so-called convective Rossby number, Ro_C, which estimates the importance of buoyant inertia relative to rotational inertia of a given system (e.g., Gilman 1977; Gilman & Foukal 1979; Aurnou et al. 2007; Brun & Palacios 2009; Soderlund et al. 2014; Soderlund 2019; Aurnou et al. 2020; Vasil et al. 2021).

Figure 1 shows normalized equatorial surface zonal velocities,

$$\alpha_e = \overline{U}_{\phi,e}/(\Omega r_o), \quad (1)$$

in stellar-like convection zone simulations from (a,b) Mabuchi et al. (2015) and (c,d) Gastine et al. (2014b). Here, $\overline{U}_{\phi,e}$ is the mean surface azimuthal velocity at the equator with overbars denoting time- and azimuthal- averaging, Ω is the mean angular rotation velocity, and r_o is the outer boundary radius. Note that α_e is synonymous with the equatorial Rossby number, Ro_e, often used in the geophysics literature. These studies, amongst others, show that there is a transition in α_e between solar-like with a prograde equatorial jet and anti-solar with a retrograde equatorial jet that occurs near a Rossby number of order unity.

In Figure 1a, the convective Rossby number, Ro_C, is plotted as the control parameter on the abscissa for hydrodynamic cases in red and magnetohydrodynamic (MHD) dynamo cases in blue. For $Ro_C \gtrsim 1$ (Aurnou et al. 2020), this parameter estimates the ratio of the rotation time scale and the buoyant free-fall time across the fluid layer, $Ro_C \simeq U_{ff}/(\Omega D)$, where $U_{ff} \simeq \sqrt{\beta \Delta T g_o D}$ is the free-fall velocity (Spiegel 1971). The convective Rossby number can be written in

★ E-mail: krista@ig.utexas.edu

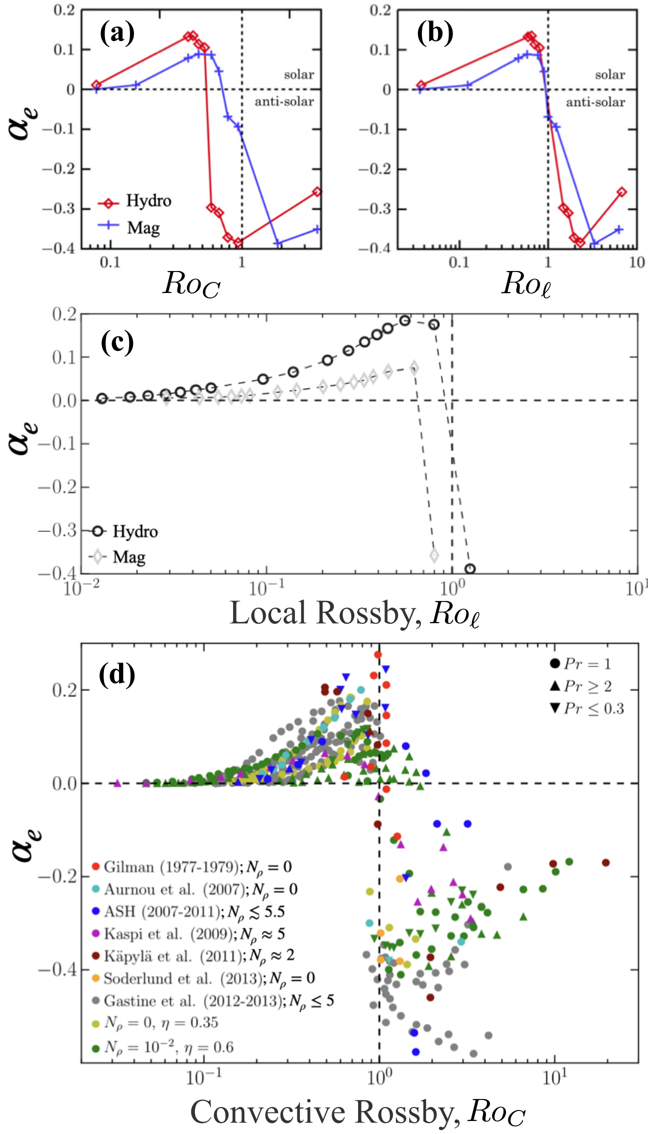

Figure 1. Comparison of differential rotation. **(a)** Equatorial surface zonal velocity, α_e, as a function of convective Rossby number, Ro_C, in hydrodynamic (red) and magnetohydrodynamic dynamo (blue) simulations with approximately three density scale heights ($N_\rho \sim 3$), adapted from Mabuchi et al. (2015). **(b)** Identical to **(a)**, but with local Rossby number, Ro_ℓ, as the abscissa. **(c)** Similar to **(b)**, but showing Boussinesq ($N_\rho = 0$) simulation results adapted from Gastine et al. (2014b). **(d)** Compilation of hydrodynamic cases with background density stratifications ranging from $N_\rho = 0$ to 5.5 and with symbol shapes denoting the value of the Prandtl number, Pr, adapted from Gastine et al. (2014b).

terms of non-dimensional control parameters as

$$Ro_C = \sqrt{\frac{RaE^2}{Pr}}, \quad \text{where } Ra = \frac{\beta g_o \Delta T D^3}{\nu\kappa}, \quad E = \frac{\nu}{\Omega D^2}, \quad Pr = \frac{\nu}{\kappa}. \tag{2}$$

The Rayleigh number Ra is a non-dimensional measure of the buoyancy forcing, the Ekman number E is the ratio of viscous to Coriolis forces, and the Prandtl number Pr is the ratio of kinematic viscosity to thermal diffusivity. Here, β is thermal expansivity, g_o is gravitational acceleration at the outer boundary, ΔT is the superadiabatic temperature difference across the shell, $D = r_o - r_i$ is shell thickness where r_i denotes the inner shell radius, ν is kinematic viscosity, and κ is thermal diffusivity. See Table 1 for a summary of non-dimensional parameter definitions.

Figure 1b shows the same α_e data plotted versus the *a posteriori* local Rossby number, defined here as

$$Ro_\ell = \frac{U}{\Omega \ell_U}, \tag{3}$$

where U is the characteristic velocity estimate and ℓ_U is the characteristic length scale of the velocity field (e.g., Christensen & Aubert 2006; Featherstone & Hindman 2016; Guervilly et al. 2019; Aurnou et al. 2020; Oliver et al. 2023). In Mabuchi et al. (2015), $U = [(3/2)\langle v_\theta^2 + v_r^2 \rangle]^{1/2}$ is the root-mean-square (rms) convective velocity with angular brackets denoting time- and volume- averaging, and they define ℓ_U based on the largest convective eddies in each simulation. We also note that Mabuchi et al. (2015) has a factor of 1/2 in their definitions of the Ekman E and Rossby Ro_ℓ numbers.

Figure 1c is adapted from Gastine et al. (2014b) and shows α_e versus Ro_ℓ with hydrodynamic cases denoted with black circles and MHD dynamo cases with grey diamonds. In this study, U is taken to be the rms non-axisymmetric contributions to the velocity field and $\ell_U = \pi D / \overline{n_U}$ is the typical flow length scale based on the kinetic-energy-weighted spherical harmonic degree $\overline{n_U}$ defined in equation (16) following Christensen (2006). The transition between solar-like and anti-solar differential rotation in panels (a - c) occurs near to a Rossby number value of order unity.

The different U and ℓ_U measurements in Mabuchi et al. (2015) and Gastine et al. (2014b) do not qualitatively change the differential rotation transition points in panels (a - c). We postulate that this insensitivity occurs because the different components of the velocity fluctuations in rapidly-rotating convection are all of the same order of magnitude (e.g., Stellmach et al. 2014; Hadjerci et al. 2024). The same holds true in non-rotating turbulent convection, in which the bulk flow is nearly isotropic (e.g., Nath et al. 2016).

Figure 1d shows hydrodynamic spherical shell convection cases that span a wide range of radial background density stratifications from Gastine et al. (2014b). This stratification is quantified through $N_\rho = \ln(\rho_i/\rho_o)$, which is the number of density scale heights across the fluid shell. Here, ρ_i (ρ_o) is the background density at the inner (outer) shell boundary. The N_ρ values range from 0 for Boussinesq cases up to approximately 5.5 in anelastic cases. Importantly, the transition between solar-like differential rotation at $Ro_C \lesssim 1$ to anti-solar differential rotation at $Ro_C \gtrsim 1$ is not strongly affected over this range of N_ρ. This implies that density stratification does not invalidate the $Ro_C \sim 1$ differential rotation regime boundary. We postulate that this occurs because the characteristic Rossby number measured across the anelastic fluid shell, and hence the effective Ro_C, does not directly depend on the mean fluid density. Instead, it is the characteristic velocity that tends to depend on density (Gilman & Foukal 1979; Gastine et al. 2013; Matilsky et al. 2019). Thus, the effects of anelastic density stratification are accounted for implicitly in the Rossby number since it is proportional to the characteristic velocity as shown, for example, in equation (3). Since the transition between anti-solar and solar-like differential rotation states seem to be largely insensitive to density stratification (in contrast to the details of the DR profile; cf., e.g., Käpylä et al. 2011; Hotta et al. 2015; Matilsky et al. 2019), our work will focus on a relatively simplistic set of Boussinesq simulations.

The modeling results shown in Figures 1(a-c) have led to the idea that magnetohydrodynamic effects are subdominant to hydrodynamic processes in large-scale convection zone dynamics. We hy-

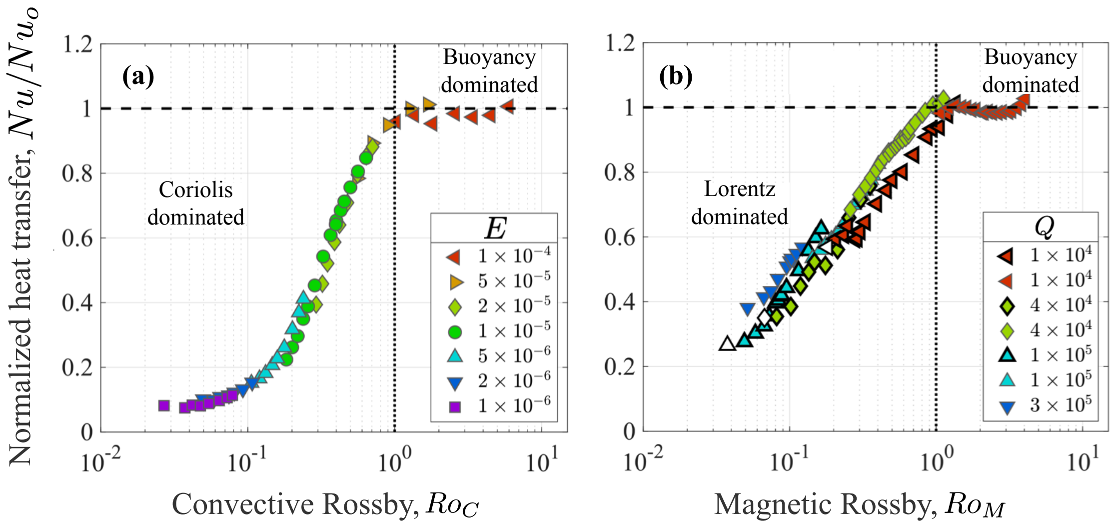

Figure 2. Comparison of normalized heat transfer, Nu/Nu_o. **(a)** Rotating (non-magnetic) convective heat transfer as a function of convective Rossby number, Ro_C; adapted from King & Aurnou (2013). Ekman number values are defined here as $E = \nu/(2\Omega D^2)$. **(b)** Magnetoconvective (non-rotating) heat transfer as a function of the magnetic Rossby number, Ro_M, defined in equation (5); adapted from Xu et al. (2023). Chandrasekhar numbers are denoted by Q.

pothesize that the idea of hydrodynamic control of convection zone transitions may be a by-product of the tendency to fix the value of electrical conductivity, σ, in these simulations. The non-dimensional form of σ is expressed via the magnetic Prandtl number:

$$Pm = \frac{\nu}{\eta} = \nu\mu_o\sigma, \tag{4}$$

where $\eta = 1/(\mu_o\sigma)$ is the magnetic diffusivity and μ_o is the magnetic permeability. The magnetic Prandtl number is often kept close to unity ($Pm \simeq 1$) in stellar and planetary dynamo modeling efforts. This characteristic fixity is a consequence of dynamo simulations being the least numerically taxing to compute in the $Pm \simeq 1$ regime (e.g., Christensen 2010; Dormy 2016). In addition, turbulent diffusivity arguments often favor setting all diffusivities to comparable values such that the turbulent diffusivity ratios are of order unity (Hotta et al. 2012; Roberts & Aurnou 2012). This turbulent diffusivity argument must, however, be treated with care: the molecular diffusivities can take on a broad range of values across stellar convection zones and, thus, it is not obvious that effective Prandtl numbers are everywhere of order unity (cf. Garaud 2021; Pandey et al. 2022; Käpylä & Singh 2022).

By fixing σ, or alternatively Pm, we posit that the strength of the Lorentz forces will tend to remain comparable in a given set of simulations. This could make it seem that MHD effects are not relevant for a given transition in the behavior of the system. However, the recent studies of Fan & Fang (2014), Karak et al. (2015), Menu et al. (2020), Brun et al. (2022), Zaire et al. (2022), Hotta et al. (2022), Käpylä (2023), Matilsky et al. (2024), and Guseva et al. (2025) (among others) all find that MHD effects cannot be neglected in convection zone dynamics. Hotta et al. (2022) even concludes that differential rotation is primarily driven by magnetic fields. Conversely, density stratification can also influence large-scale dynamo behavior, favoring multipolar over dipolar solutions at sufficiently strong stratification (e.g., Gastine et al. 2012), and enabling magnetic pumping to induce complex time variations in dipolar fields (e.g., Guseva et al. 2025). Stratification may also affect the propagation direction of dynamo waves (e.g., Käpylä et al. 2013).

Thus far, we have focused on transitions in zonal flow behavior. However, transitions in convective heat transfer have also been used to denote changes in global-scale behavioral dynamics (e.g., Glazier et al. 1999; Elliott et al. 2000; Balbus 2009; King et al. 2009; Plumley & Julien 2019; Matilsky et al. 2020; Xu et al. 2023). This assumes that the mean heat transfer is a byproduct of all the collective convective motions that occur in a given fluid layer. Thus, changes in heat transfer scaling behaviors are argued to be interrelated to changes in large-scale dynamics. In laboratory experiments where velocity field data has not been acquired (e.g., Grannan et al. 2022), it is necessary to make use of this heat transfer ansatz in order to cross-compare the convection regimes in these systems.

Figure 2 shows laboratory convective heat transfer measurements in a liquid gallium-filled cylinder heated from below and cooled from above as a function of (a) applied rotation rate and (b) applied magnetic field strength, adapted from King & Aurnou (2013) and Xu et al. (2023). The convective heat transfer data, Nu, is normalized in both panels by the heat transfer measured in non-rotating, non-magnetic convection experiments, Nu_o. The rotating convection data in Figure 2a shows that the convective heat transfer is reduced when $Ro_C \lesssim 1$. In this regime, rotation dominates over buoyancy-driven inertia and the flow becomes strongly rotationally-constrained (e.g., Julien & Knobloch 2007). It is found that $Nu/Nu_o \approx 1$ when $Ro_C \gtrsim 1$, showing that the convective flow is no longer constrained by rotation when the buoyancy-driven inertial forces exceed the Coriolis forces.

The low magnetic Reynolds number ($Rm = UD/\eta \ll 1$), liquid metal, laboratory magnetoconvection data shown in Figure 2b is similar in gross structure to that of Figure 2a. The abscissa in Figure 2b shows the magnetic Rossby number, which is the analog to Ro_C given liquid metal, laboratory MHD conditions:

$$Ro_M = \sqrt{\frac{RaQ^{-2}}{Pr}}, \quad \text{where } Q = \frac{\sigma B^2 D^2}{\rho\nu}. \tag{5}$$

The Chandrasekhar number Q estimates the ratio of Lorentz and viscous forces, with ρ denoting the fluid density and B denoting the strength of the magnetic field (externally imposed in low-Rm lab experiments, as opposed to high-Rm dynamo simulations where magnetic field properties are not known *a priori*). In comparing rotating and magnetoconvection systems, Q^{-1} is the MHD analog to E.

Further, the interaction parameter N is often employed in the MHD literature (e.g., Sommeria & Moreau 1982), where $N^{-1} = Ro_M$.

The magnetic Rossby number defined in (5) characterizes the ratio of inertial and Lorentz forces in the low-*Rm*, *quasi-static limit* in which induced fields are negligible and the current density can be estimated via Ohm's Law, $\mathbf{J} = \sigma(-\nabla\phi + \mathbf{u}\times\mathbf{B})$ where ϕ is electrical potential (e.g., Davidson 2001; Sarris et al. 2006; Yan et al. 2019; Xu et al. 2023; Horn & Aurnou 2024). Thus, it is not necessary to solve the magnetic induction equation to calculate the Lorentz forces in this limit. In rotating systems, the magnetic Rossby number can be recast as

$$Ro_M = \frac{Ro_C}{\Lambda}, \quad \text{where} \quad \Lambda = \frac{\sigma B^2}{\rho\Omega}. \tag{6}$$

Here, Λ is the traditional form of the Elsasser number that estimates the ratio of Lorentz and Coriolis forces also in the low-*Rm*, quasi-static MHD limit (e.g., Cardin et al. 2002; Soderlund et al. 2015; Dormy 2016; Aurnou & King 2017; Horn & Aurnou 2022).

The normalized heat transfer in Figure 2b is decreased in the $Ro_M \lesssim 1$ regime, which shows that the quasi-static, low-*Rm* Lorentz force constrains the convective turbulence when it exceeds the strength of the inertial forces (e.g., Julien & Knobloch 2007). The similarities in zeroth-order structure of the data in Figures 2a,b imply that Coriolis forces and Lorentz forces are both capable of changing the global-scale convection dynamics, which are parameterized in this figure by the normalized, global heat transferred through the fluid layer.

2 LOCAL MAGNETIC ROSSBY NUMBER

We hypothesize that grossly similar behavioral transitions also exist in high-*Rm* spherical dynamo systems as are found in Figure 2. We predict that convection zone dynamics in spherical shell dynamo models will undergo regime transitions as a function of both the Rossby number and the high-*Rm* form of the magnetic Rossby number. As discussed above, it is well known that Ro_C correlates with changes in convection zone dynamics. We will, therefore, focus in this study on determining the conditions under which changes in Lorentz forces alter the convection zone dynamical regime.

The magnetic Rossby number Ro_M cannot, however, be employed to interpret dynamo modeling results since Ro_M holds in the low-*Rm*, quasi-static limit whereas $Rm > \mathcal{O}(10)$ in dynamo systems (Roberts & King 2013). Further, Ro_M is not a well-defined control parameter in dynamo simulations; it cannot be calculated *a priori* since the magnetic field properties are not known before running a given dynamo simulation. This differs from the laboratory magnetoconvection experiments shown in Figure 2b in which the magnetic field is applied by an external electromagnet.

In order, then, to interpret our dynamo simulation results, it is necessary to formulate a generalized form of the magnetic Rossby number that is valid in $Rm > 1$ dynamo settings. Following Soderlund et al. (2015), the current density $\mathbf{J} = (\nabla\times\mathbf{B})/\mu_o$ is employed. This form of $\mathbf{J}$ is accurate for all *Rm* values so long as the MHD approximation holds, in which displacement currents can be neglected (Davidson 2001). Here, velocity and magnetic field gradient operators are scaled in terms of ℓ_U^{-1} and ℓ_B^{-1}, respectively (see Table 2 for definitions used in the literature). This generalized, local-scale, magnetic Rossby number then takes the form

$$Ro_{M,\ell} = \frac{|\rho\mathbf{u}\cdot\nabla\mathbf{u}|}{|[(\nabla\times\mathbf{B})/\mu_o]\times\mathbf{B}|} \approx \frac{U^2/\ell_U}{[B^2/(\rho\mu_o)]/\ell_B} \approx \left(\frac{U^2}{V_A^2}\right)\left(\frac{\ell_B}{\ell_U}\right) \tag{7}$$

where $V_A = \sqrt{B^2/(\rho\mu_o)}$ is the Alfvén velocity (Schaeffer et al. 2012).

Based on the rightmost expression in equation (7), the local magnetic Rossby number $Ro_{M,\ell}$ is seen to be the kinetic to magnetic energy density ratio (U^2/V_A^2) modified by the ratio of dynamical length scales (ℓ_B/ℓ_U). Thus, if $\ell_B \approx \ell_U$, the ratio of the inertial and Lorentz forces is well approximated by the energy density ratio. In cases where ℓ_B and ℓ_U are not comparable, as can occur in dynamo simulations in which *Pm* is not close to unity (e.g., Schekochihin et al. 2004; Ponty et al. 2005; Schaeffer et al. 2017; Guilet et al. 2022), the inclusion of the (ℓ_B/ℓ_U) term in $Ro_{M,\ell}$ is obligatory.

Accurate *a priori* estimates of B, U, ℓ_U, and ℓ_B are difficult to make in turbulent dynamo systems. Thus, we recast $Ro_{M,\ell}$ in terms of measurable *a posteriori* output parameters, the local Rossby number Ro_ℓ and the local Elsasser number Λ_ℓ, to obtain a generalized (non-quasi-static, non-low *Rm*) definition:

$$Ro_{M,\ell} = \frac{Ro_\ell}{\Lambda_\ell}, \quad \text{where} \quad \Lambda_\ell = V_A^2/(U\Omega\ell_B). \tag{8}$$

We stress that $Ro_{M,\ell}$ is not a control parameter, unlike Ro_M, since $Ro_{M,\ell}$ can only be calculated after a given dynamo simulation run has completed.

Figure 3 provides an example of the utility of $Ro_{M,\ell}$ using data harvested from published datasets (Gastine et al. 2012; Soderlund et al. 2012; Yadav et al. 2016a; Menu et al. 2020) and this study. The ordinate in all four panels denotes the values of dipolarity, f_D, defined in Soderlund et al. (2012) as the ratio of the dipole to total magnetic energy on the model's outer spherical boundary (see Table 1). We note that other dipolarity definitions are also used in the literature as summarized in Table 2 for the studies included here. Here, dipolar magnetic field morphologies are defined to have $f_D \gtrsim 0.1$ and multipolar morphologies to have $f_D \lesssim 0.1$.

Figures 3a,b show that the rotational and magnetic control parameters Ro_C and Ro_{QS}^M, respectively, are non-elucidatory here since the dipolarity values are rather strongly scattered in both panels. Further, the *a posteriori* local diagnostic parameter Ro_ℓ is also unable to reduce the spread of f_D data in Figure 3c, despite $Ro_\ell \sim 0.1$ often serving as a proxy for predicting dipolar versus multipolar dynamos (e.g, Christensen & Aubert 2006; Dormy 2025; Tikoo & Evans 2022). The local magnetic Rossby number $Ro_{M,\ell}$, plotted along the abscissa in Figure 3d, better collapses the f_D data, with dipolar solutions corresponding to strong local-scale Lorentz forces and multipolar solutions clustered in the vicinity of $Ro_{M,\ell} \gtrsim 0.5$ where the inertial and magnetic forces are approximately in balance. Thus, Figure 3 demonstrates the potential diagnostic capabilities and relevance of $Ro_{M,\ell}$ in analyzing the physics of dynamo systems.

The goal of this study is to show that the regimes of spherical shell dynamo physics are controlled by a local-scale, multi-term MHD balance dominated by the Coriolis, Lorentz, and inertial terms using a suite of dynamo simulations. Because one cannot calculate $Ro_{M,\ell}$ *a priori*, we hold all control parameters fixed except for the magnetic Prandtl number, $Pm \propto \sigma$, in our dynamo simulations. This allows us to study how the relative strength of the Lorentz force correlates with the dynamo morphology and differential rotation in our models. We find distinct behavioral states as a function of $Ro_{M,\ell}$. This implies that not only is the convective Rossby number important to the large-scale convection zone dynamics, but that its MHD counterpart, the local magnetic Rossby number $Ro_{M,\ell}$, is of dynamical importance in dynamo systems as well.

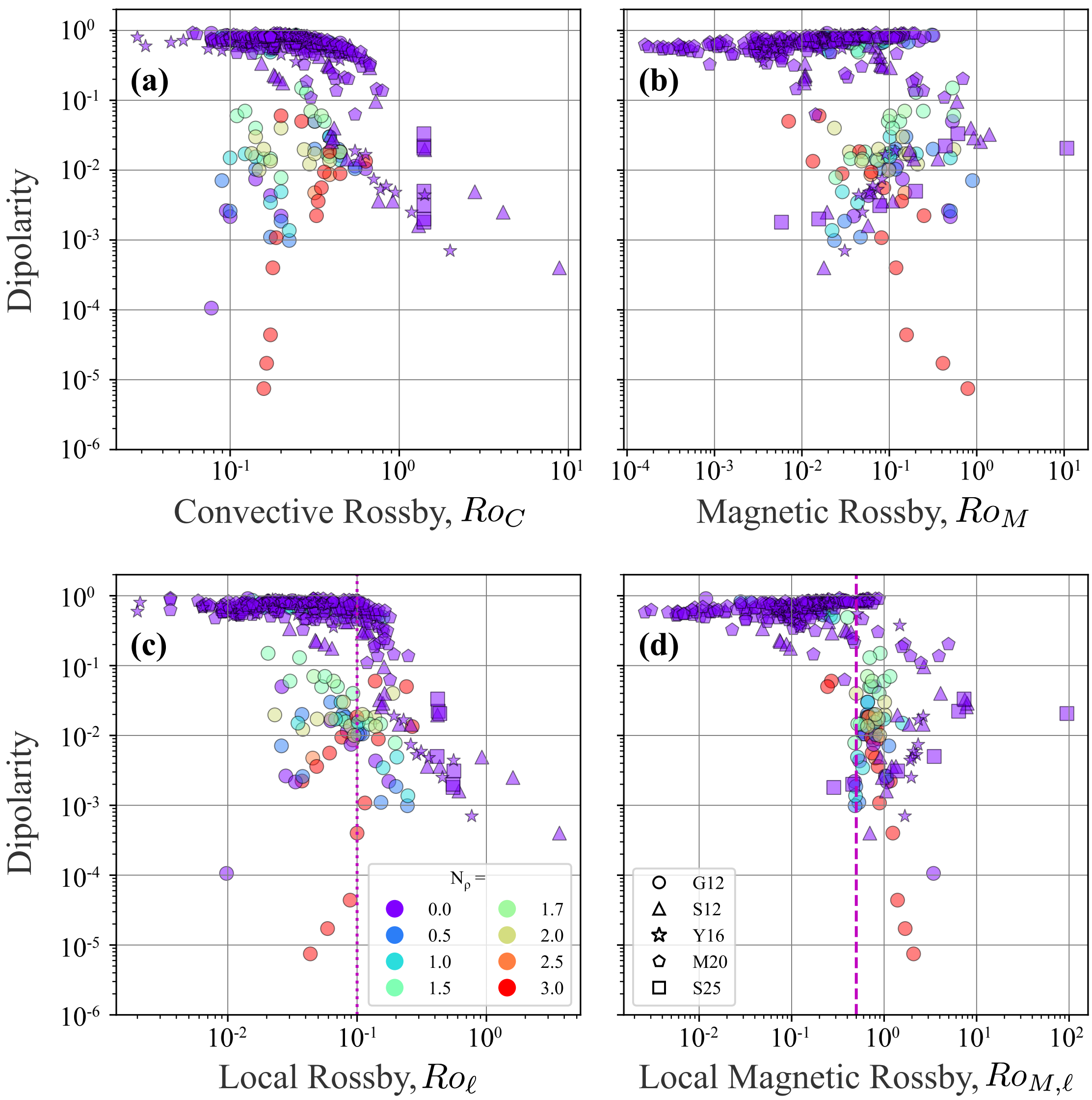

Figure 3. Dipolarity, f_D, with data from Gastine et al. (2012) (G12); Soderlund et al. (2012) (S12); Yadav et al. (2016a) (Y16); Menu et al. (2020) (M20); and this study (S25), as a function of **(a)** convective Rossby number, Ro_C, **(b)** magnetic Rossby number, Ro_M, **(c)** local Rossby number, Ro_ℓ, and **(d)** local magnetic Rossby number, $Ro_{M,\ell}$. Shape denotes the source publication, and color refers to density stratification, N_ρ. Definitions for f_D, Ro_ℓ, and Λ_ℓ used to calculate $Ro_{M,\ell}$ differ between studies, as described in Table 2; model set-ups also differ between these studies (e.g., both stress-free and no-slip models are shown).

3 METHODS

We use the open-source, pseudospectral dynamo code MagIC (Wicht 2002; Gastine & Wicht 2012) with the SHTns library to efficiently calculate the spherical harmonic transforms (Schaeffer 2013). The models carried out here simulate three-dimensional (3D), time-dependent, thermally-driven convection of a Boussinesq fluid in a spherical shell rotating with constant angular velocity $\Omega\hat{\mathbf{z}}$. The shell's geometry is set to $\chi = r_i/r_o = 0.35$ with boundaries that are isothermal, impenetrable, and stress-free. The inner sphere, $r < r_i$, is treated as a solid that has the same electrical conductivity as the fluid shell, the outer boundary of which is electrically insulating. Gravity varies linearly with spherical radius. The dimensionless governing equations for this system are

$$E\Big(\underbrace{\frac{\partial\mathbf{u}}{\partial t}}_{F_U}+\underbrace{\mathbf{u}\cdot\nabla\mathbf{u}}_{F_I}-\underbrace{\nabla^2\mathbf{u}}_{F_D}\Big)+\underbrace{2\hat{\mathbf{z}}\times\mathbf{u}}_{F_C}+\underbrace{\nabla p}_{F_P}=\underbrace{\frac{RaE}{Pr}\frac{\mathbf{r}}{r_o}T}_{F_B}+\underbrace{\frac{1}{Pm}(\nabla\times\mathbf{B})\times\mathbf{B}}_{F_L}, \tag{9}$$

$$\frac{\partial\mathbf{B}}{\partial t}=\nabla\times(\mathbf{u}\times\mathbf{B})+\frac{1}{Pm}\nabla^2\mathbf{B}, \tag{10}$$

$$\frac{\partial T}{\partial t}+\mathbf{u}\cdot\nabla T=\frac{1}{Pr}\nabla^2 T, \tag{11}$$

$$\nabla\cdot\mathbf{u}=0,\quad \nabla\cdot\mathbf{B}=0, \tag{12}$$

Parameter	Definition	Interpretation
Rayleigh number	$Ra = \frac{\beta g \Delta T D^3}{\nu\kappa} = 2.22 \times 10^7$	Buoyancy / Diffusion
Ekman number	$E = \frac{\nu}{\Omega D^2} = 3.0 \times 10^{-4}$	Viscous / Coriolis forces
Prandtl number	$Pr = \frac{\nu}{\kappa} = 1$	Kinematic viscosity / Thermal diffusivity
Magnetic Prandtl number	$Pm = \frac{\nu}{\eta} = \mu_o \sigma \nu = [10, 5, 2, 1, 0.75, 0.50, 0.25, 0]$	Kinematic viscosity / Magnetic diffusivity
Radius ratio	$\chi = \frac{r_i}{r_o} = 0.35$	Shell geometry
Reynolds number	$Re = \frac{UD}{\nu} = \sqrt{2\mathcal{E}_K}$	Inertial / Viscous forces
Magnetic Reynolds number	$Rm = \frac{UD}{\eta} = RePm$	Magnetic induction / Magnetic diffusion
Equatorial surface Rossby number	$\alpha_e = \frac{\overline{U}_{\phi,e}}{\Omega r_o}$	Normalized equatorial zonal velocity (outer boundary)
Rossby number	$Ro = \frac{U}{\Omega D} = ReE$	Inertial / Coriolis forces (global)
Local Rossby number	$Ro_\ell = \frac{U}{\Omega \ell_U} = Ro \frac{D}{\ell_U}$	Inertial / Coriolis forces (local)
Convective Rossby number	$Ro_C = \frac{\sqrt{\beta \Delta T g_o D}}{\Omega D} = \sqrt{RaE^2/Pr}$	Buoyant inertial / Coriolis forces (global)
Magnetic Rossby number	$Ro_M = \frac{\rho\sqrt{\beta \Delta T g_o D}}{\sigma B^2 D} = \sqrt{RaQ^{-2}/Pr} = Ro_C/\Lambda$	Buoyant inertial / Lorentz forces (global)
Local magnetic Rossby number	$Ro_{M,\ell} = \frac{\rho \mu_0 \ell_B U^2}{\ell_U B^2} = \left(\frac{U^2}{V_A^2}\right)\left(\frac{\ell_B}{\ell_U}\right) = Ro_\ell/\Lambda_\ell$	Buoyant inertial / Lorentz forces (local)
	$V_A = \sqrt{B^2/(\rho\mu_o)}$	Alfvén velocity
Chandrasekhar number	$Q = \frac{\sigma B^2 D^2}{\rho\nu}$	Lorentz / Viscous forces (low-Rm)
Elsasser number	$\Lambda = \frac{\sigma B^2}{\rho\Omega} = QE = \mathcal{E}_M PmE$	Lorentz / Coriolis forces (low-Rm)
Local Elsasser number	$\Lambda_\ell = \frac{B^2}{\rho\mu_o\Omega U \ell_B} = \frac{V_A^2}{U\Omega\ell_B} = \frac{\Lambda}{Rm}\frac{D}{\ell_B}$	Lorentz / Coriolis forces (high-Rm)
Force integral	$F = \int_V \left(\mathcal{F}_r^2 + \mathcal{F}_\theta^2 + \mathcal{F}_\phi^2\right)^{1/2} dV$	Volume-integrated RMS forces
Nusselt number	$Nu = \frac{r_o}{r_i}\frac{qD}{\rho C_p \kappa \Delta T}$	Total / Conductive heat transfer
Dipolarity	$f_D = \frac{\mathcal{P}(n=1, m=0, r=r_o)}{\sum_{n=1}^{n=n_{max}} \mathcal{P}(n,\ r=r_o)}$	Magnetic power in axial dipole / Total magnetic power
Energies	$\mathcal{E}_K = \frac{1}{2V_s}\int \mathbf{u}\cdot\mathbf{u}\, dV$	Kinetic energy density
	$\mathcal{E}_M = \frac{1}{2V_s}\int \mathbf{B}\cdot\mathbf{B}\, dV$	Magnetic energy density
	$\overline{n_U} = \sum n\langle \mathbf{u}_n \cdot \mathbf{u}_n\rangle / \langle \mathbf{u}\cdot\mathbf{u}\rangle$	Characteristic degree of the velocity field
	$\overline{n_B} = \sum n\langle \mathbf{B}_n \cdot \mathbf{B}_n\rangle / \langle \mathbf{B}\cdot\mathbf{B}\rangle$	Characteristic degree of the magnetic field
	$\overline{m_U} = \sum m\langle \mathbf{u}_m \cdot \mathbf{u}_m\rangle / \langle \mathbf{u}\cdot\mathbf{u}\rangle$	Characteristic order of the velocity field
Spatial	$\overline{m_B} = \sum m\langle \mathbf{B}_m \cdot \mathbf{B}_m\rangle / \langle \mathbf{B}\cdot\mathbf{B}\rangle$	Characteristic order of the magnetic field
descriptors	$\overline{k_U} = \sqrt{\overline{n_U}^2 + \overline{m_U}^2}$	Characteristic wavenumber of the velocity field
	$\overline{k_B} = \sqrt{\overline{n_B}^2 + \overline{m_B}^2}$	Characteristic wavenumber of the magnetic field
	$\ell_U/D = \pi/\overline{n_U}$	Characteristic length scale of the velocity field
	$\ell_B/D = \pi/(2\overline{k_B})$	Characteristic length scale of the magnetic field

Table 1. Summary of non-dimensional parameters. Symbols are defined in the text. Note that a comparison of dipolarity and length scale definitions used in the literature compiled in our study are given in Table 2.

where **u** is the velocity vector, **B** is the magnetic induction vector, T is the temperature, and p is the non-hydrostatic pressure. We make use of typical non-dimensionalizations used in the planetary dynamo literature: D as length scale; ΔT as temperature scale; $\tau_\nu \sim D^2/\nu$ as time scale; $\rho\nu\Omega$ as pressure scale; ν/D as velocity scale such that the non-dimensional rms flow speed is equal to the Reynolds number $Re = UD/\nu$; and $\sqrt{\rho\mu_o\eta\Omega}$ as magnetic induction scale such that the square of the non-dimensional rms magnetic field strength is equal to the traditionally-defined Elsasser number Λ (cf. Cardin et al. 2002; Soderlund et al. 2015).

The governing non-dimensional parameters are the radius ratio χ, the magnetic Prandtl number Pm, the thermal Prandtl number Pr, the Ekman number E, and the Rayleigh number Ra (see Eqs. 2 and 4). For all models carried out herein, we use fixed values of $E = 3.0 \times 10^{-4}$, $Ra = 2.22 \times 10^7$, $Pr = 1$, and $\chi = 0.35$. These parameters correspond to a critical Rayleigh number of $Ra_C = 2.08 \times 10^6$

Publication	ℓ_U/D	ℓ_B/D	f_D numer.	f_D denom.
S12	$\frac{\pi}{\sqrt{\bar{n}_U^2+\bar{m}_U^2}}$	$\frac{\pi}{2\sqrt{\bar{n}_B^2+\bar{m}_B^2}}$	$\mathcal{P}(n=1)$	$\Sigma_{n=1}^{n_{max}}\mathcal{P}(n)$
G12	$\frac{\pi}{\bar{n}_U}$	$\frac{\pi}{2\sqrt{\bar{n}_B^2+\bar{m}_B^2}}$	$\mathcal{P}(n=1,m=0)$	$\Sigma_{n=1}^{n_{max}}\mathcal{P}(n)$
Y16	$\frac{\pi}{\bar{n}_U}$	$\frac{\pi}{2\bar{n}_B}$	$\mathcal{P}(n=1,m=0)$	$\Sigma_{n=1}^{n_{max}}\mathcal{P}(n)$
D16	$\frac{\pi}{\bar{n}_U}$	$\sqrt{\frac{\int_V \boldsymbol{B}^2 dV}{\int_V (\nabla\times\boldsymbol{B})^2 dV}}$	$\mathcal{P}(n=1,m=0)$	$\Sigma_{n=1}^{n=12}\mathcal{P}(n)$
M20	$\frac{\pi}{\bar{n}_U}$	$\sqrt{\frac{\int_V \boldsymbol{B}^2 dV}{\int_V (\nabla\times\boldsymbol{B})^2 dV}}$	$\mathcal{P}(n=1)$	$\Sigma_{n=1}^{n=12}\mathcal{P}(n)$
T23	$\frac{\pi}{\bar{n}_U}$	$\sqrt{\frac{\int_V \boldsymbol{B}^2 dV}{\int_V (\nabla\times\boldsymbol{B})^2 dV}}$	$\mathcal{P}(n=1,m=0)$	$\Sigma_{n=1}^{n=12}\mathcal{P}(n)$
S25	$\frac{\pi}{\bar{n}_U}$	$\frac{\pi}{2\sqrt{\bar{n}_B^2+\bar{m}_B^2}}$	$\mathcal{P}(n=1,m=0)$	$\Sigma_{n=1}^{n_{max}}\mathcal{P}(n)$

Table 2. Length scales used to calculate Ro_ℓ and Λ_ℓ, and definition of dipolarity f_D on the outer boundary, split into numerator (indicating total dipole or axial dipole power) and denominator (relative to the power in the spectrum up to a specified degree n) for the studies shown in Figures 3 and 9. Publication sources include Soderlund et al. (2012) (S12); Gastine et al. (2012) (G12); Yadav et al. (2016a) (Y16); Dormy (2016) (D16); Menu et al. (2020) (M20); Teed & Dormy (2023) (T23); and this study (S25).

(Soderlund et al. 2013; Barik et al. 2023), yielding a supercriticality of $Ra/Ra_{crit} \sim 110$, and a fixed convective Rossby number value of $Ro_C = 1.4$ for all our simulations. For $Ro_C \gtrsim 1$, the buoyancy forces tend to overwhelm the Coriolis forces, generating quasi-3D convective turbulence which typically act to generate anti-solar differential rotation profiles (e.g., Figure 1; Aurnou et al. 2007; Soderlund et al. 2013; Gastine et al. 2013; Gastine et al. 2014b; Featherstone & Miesch 2015; Mabuchi et al. 2015; Soderlund 2019; Camisassa & Featherstone 2022). We have purposefully chosen to fix $Ro_C \approx 1$ in order to be close to the rotationally-controlled zonal flow transition point.

This choice of $Ro_C \approx 1$ should position our dynamo survey such that it is sensitive to magnetically-controlled dynamical transitions. Towards this end, we systematically vary the electrical conductivity such that $Pm = [10, 5, 2, 1, 0.75, 0.50, 0.25, 0]$, noting that no dynamos are sustained for $Pm \lesssim 0.2$. As shown in Figure 4 and Table 3, the resulting $Ro_{M,\ell}$ values range from 0.3 to 94 and thus cross unity, where a transition may be most intuitive.

The choice of a Boussinesq fluid in a thick fluid shell with isothermal boundary conditions defines as simple a system as could be created for this problem, both physically and computationally. We argue that this simplified approach is appropriate for identifying zeroth-order hydrodynamic regime transitions (e.g., Gilman 1977; Aurnou et al. 2007), as prior studies have shown that such transitions exhibit only weak to moderate sensitivity to anelastic effects, shell geometry, and the nature of buoyancy forcing (e.g., Gastine et al. 2013, 2014a; Gastine et al. 2014b; Featherstone & Miesch 2015; Gastine & Aurnou 2023; Lemasquerier et al. 2023). In contrast, dynamo simulations exhibit some sensitivity to both MHD effects and anelasticity (e.g., Karak et al. 2015; Hotta et al. 2022; Zaire et al. 2022), though the full parameter space remains poorly characterized.

The models use 192 spherical harmonic modes, 65 radial levels in the outer shell, and 17 radial levels in the inner core. No azimuthal symmetries or hyperdiffusivities are employed. All cases are initialized either using the results of prior dynamo models with different Pm values or from random thermal perturbations and a seed magnetic field; the choice of initial conditions was found to have no significant effect on the results. This lack of hysteresis is consistent with other MHD studies (e.g., Karak et al. 2015), in contrast to the bistability identified in hydrodynamic simulations (e.g., Gastine et al. 2014b; Käpylä et al. 2014). Once the initial transient behavior has subsided, the model results are all time-averaged over a time window Δt. This corresponds to the non-dimensional averaging time $\Delta t_\nu = \frac{\Delta t}{\tau_\nu} = C = 0.09$ measured in viscous diffusion time units. Expressing this non-dimensional averaging window in magnetic diffusion times ($\tau_\eta = D^2/\eta$) and convective overturn times ($\tau_U = D/U$), respectively, yields

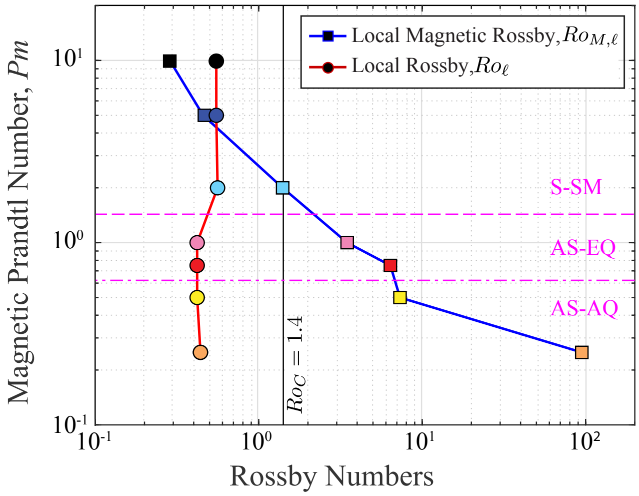

Figure 4. Local magnetic Rossby $Ro_{M,\ell}$ (blue line) and local Rossby Ro_ℓ (red line) numbers versus the magnetic Prandtl number, Pm (also denoted by color). For comparison, the fixed convective Rossby number of $Ro_C = 1.4$ is denoted by the black line. The dynamo regimes are further marked with pink labels.

$$\Delta\tau_\eta = \frac{\Delta t}{\tau_\eta} = \frac{\Delta t}{\tau_\nu}\frac{\tau_\nu}{\tau_\eta} = C\,\frac{\eta}{\nu} = 0.09\,Pm^{-1}\,, \tag{13}$$

$$\Delta t_U = \frac{\Delta t}{\tau_U} = \frac{\Delta t}{\tau_\nu}\frac{\tau_\nu}{\tau_U} = C\,\frac{UD}{\nu} = 0.09\,Re\,. \tag{14}$$

Thus, Δt_η ranges from 0.009 to 0.4 and the associated Δt_U values range from 39 to 97 (see Table 3).

4 RESULTS

As we will demonstrate, changing only the electrical conductivity of the fluid, as represented by Pm (*a priori*) and $Ro_{M,\ell}$ (*a posteriori*), leads to first-order changes in the velocity and magnetic fields. We identify two types of differential rotations — solar-like (S) and anti-solar (AS) — and three types of magnetic field morphologies — strongly-multipolar (SM), equatorial quadrupole (EQ), and axial quadrupole (AQ). These combine to define three dynamical regimes: S-SM (solar-like, strongly multipolar), AS-EQ (anti-solar, equatorial quadrupole), and AS-AQ (anti-solar, axial quadrupole) as summarized inTable 4.

4.1 Heat Transfer Efficiency

Heat transfer efficiency is measured by the Nusselt number, which is the ratio of total to conductive heat flux across the shell:

$$Nu = \frac{r_o}{r_i}\frac{qD}{\rho C_p \kappa \Delta T} \tag{15}$$

Regime	Pm	$Ro_{M,\ell}$	Rm	Re	$Re_{m>0}$	Ro	Ro_l	α_e	ℓ_U	ℓ_B	ℓ_U/ℓ_B	Nu	f_D	Λ_i	Λ_l	$\mathcal{E}_M\,/\,\mathcal{E}_K$	$\langle F_I\rangle/\langle F_L\rangle$
S-SM	10	0.287	4348	435	418	0.130	0.551	+0.041	0.237	0.029	8.25	12.8	0.0018	240	1.92	0.42	0.394
S-SM	5	0.459	2263	453	417	0.136	0.552	+0.062	0.246	0.033	7.45	12.7	0.0020	90	1.20	0.29	0.662
S-SM	2	1.40	1068	534	457	0.160	0.561	+0.076	0.286	0.042	6.86	12.6	0.0031	18	0.400	0.10	1.72
AS-EQ	1	3.45	986	986	754	0.296	0.416	-0.287	0.711	0.058	12.2	13.5	0.0050	7.0	0.121	0.024	3.68
AS-EQ	0.75	6.45	756	1008	735	0.302	0.423	-0.303	0.714	0.064	11.1	13.3	0.0222	3.2	0.066	0.014	6.55
AS-AQ	0.50	7.31	499	998	697	0.299	0.419	-0.313	0.714	0.082	8.76	13.1	0.0332	2.3	0.057	0.016	8.27
AS-AQ	0.25	93.7	269	1077	692	0.323	0.435	-0.341	0.743	0.104	7.14	13.1	0.0206	0.13	0.005	0.002	87.8
AS	0	–	–	1088	677	0.326	0.436	-0.346	0.749	–	–	13.0	–	–	–	–	–

Table 3. Diagnostic parameters for variable Pm cases all with fixed $\chi = r_i/r_o = 0.35$ and $Ro_C = 1.4$ (corresponding to $Ra = 2.22\times10^7$, $E = 3.0\times10^{-4}$, and $Pr = 1$). Parameters are defined in Table 1; the rightmost column gives the ratio of volume-integrated inertial forces, $\langle F_I\rangle$, and Lorentz forces, $\langle F_L\rangle$. Dynamo models with $Pm \geq 2$ are in the solar-like differential rotation, strongly multipolar magnetic field (S-SM) regime; models with $Pm = [0.75, 1]$ are in the anti-solar, equatorial quadrupole (AS-EQ) regime; models with $Pm \leq 0.5$ are in the anti-solar, axial quadrupole (AS-AQ) regime.

Regime ($Ro_{M,\ell}$)	Differential rotation	Magnetic field morphology	Interpretation
S-SM ($Ro_{M,\ell} \lesssim 1.4$)	Solar-like	Strongly-Multipolar	Lorentz dominated
AS-EQ ($3.5 \lesssim Ro_{M,\ell} \lesssim 6.4$)	Anti-Solar	Equatorial Quadrupole	
AS-AQ ($Ro_{M,\ell} \gtrsim 7.3$)	Anti-Solar	Axial Quadrupole	Buoyancy dominated

Table 4. Definition of regimes identified in our study with fixed $Ro_C = 1.4$ based on the differential rotation and magnetic field characteristics.

where q is heat flux per unit area on the outer shell boundary and C_p is specific heat capacity (see also Yadav et al. (2016b)). Since ΔT is fixed in our simulations, the conductive heat flux, which is proportional to $\Delta T/D$, is fixed. Changes in Nu thus reflect variations in the amount of thermal energy transferred convectively across the shell. The Nusselt number ranges from $Nu = 12.6$ in the S-SM regime to $Nu = 13.5$ in the AS-EQ regime (Table 3). Comparing against the non-magnetic value of $Nu = 13.1$, the dynamo can therefore act to either slightly diminish or slightly enhance the convective component of the heat transfer, depending on the value of the local magnetic Rossby number. These $Nu > 10$ values and relatively small changes across the survey are consistent with the supercriticalities of the models exceeding 100.

4.2 Velocity Fields

Two distinct styles of zonal flow are found in our fixed $Ro_C = 1.4$ survey. As shown in Figure 5a, solar-like differential rotation with a strong retrograde equatorial jet and flanking prograde jets form when $Pm \leq 1$. In contrast, zonal flows in models with $Pm \geq 2$ are anti-solar, where a broad prograde equatorial jet dominates with retrograde flow near and interior to the tangent cylinder. Wind speeds in the prograde jet regime are only about half those in the retrograde jet regime.

Figure 5b illustrates the azimuthally-averaged zonal flows and meridional circulations for three representative electrical conductivity values. In all cases, these zonal flows are largely invariant in the direction parallel to the rotation axis. Each hemisphere also develops two large circulation cells that are of opposite sense across the equator. The models with anti-solar DR have relatively strong cells with polar upwelling within the tangent cylinder, which is the imaginary axial cylinder that circumscribes the inner shell boundary's equator (e.g., Aurnou et al. 2003); these polar cells are much less pronounced in the solar-like DR cases. The circulation patterns also differ at large cylindrical radii: while smaller cells near the outer shell boundary occur in both regimes, their directions of rotation are reversed.

Figure 5c shows α_e, the zonal velocity on the outer boundary at the equator as defined in equation (1), as a function of $Ro_{M,\ell}$. Here, we see that the flip in sign of α_e occurs for $Ro_{M,\ell} \simeq 1$, reminiscent of the change in zonal flow direction near $Ro_C \simeq 1$ shown in Figure 1. Figure 5 thus demonstrates that magnetic field effects, as measured by $Ro_{M,\ell}$, can flip the convection zone's differential rotation profile from solar-like to anti-solar states (see also Fan & Fang 2014).

These trends are also reflected in globally-averaged quantities. Despite the convective Rossby number being fixed at $Ro_C \sim 1$, the Reynolds numbers differ by more than a factor of two across the survey (Table 3). Decomposing the Reynolds number into axisymmetric and non-axisymmetric components, $Re = Re_{m=0} + Re_{m>0}$, shows that the velocity field is predominantly non-axisymmetric with $Re_{m>0}/Re > 0.85$ at low $Ro_{M,\ell} \leq 1.4$ values. This ratio decreases with increasing $Ro_{M,\ell}$ values, reaching $Re_{m>0}/Re = 0.64$ in the highest $Ro_{M,\ell} = 94$ case such that axisymmetric contributions become more significant. This contrast between global and non-axisymmetric Reynolds numbers indicates differences in the differential rotation and, secondarily, meridional circulations.

A notably smaller variation in the local Rossby number is found across the survey, spanning $Ro_l \sim 0.5 \pm 0.1$ (Figure 4). Here, Ro_ℓ, computed here assuming the Gastine et al. (2012) definition for typical flow length scale:

$$\ell_U/D = \pi/\overline{n_U}, \quad \text{where} \quad \overline{n_U} = \sum_{n=1}^{n_{max}} \frac{n\langle \mathbf{u}_n \cdot \mathbf{u}_n\rangle}{\langle \mathbf{u}\cdot\mathbf{u}\rangle}. \tag{16}$$

The Ro_ℓ values vary less because flow speed increases (Re) are largely offset by increases in flow length scale (ℓ_U). The velocity field is larger-scale in models with $Ro_{M,\ell} > 1$, where $\ell_U/D \sim 0.72$ on average, compared to those with $Ro_{M,\ell} \lesssim 1$ where $\ell_U/D \sim 0.26$ (Table 3).

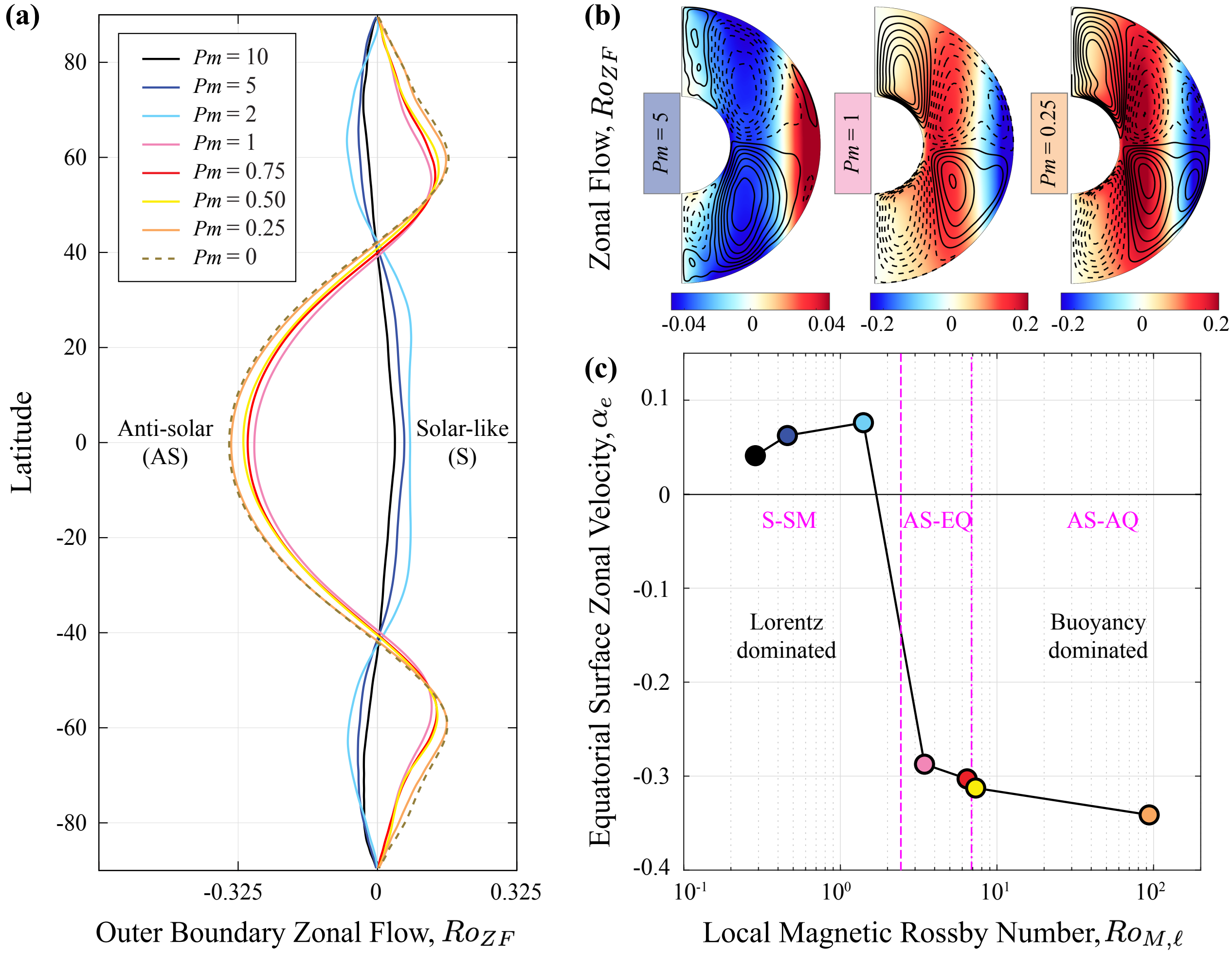

Figure 5. Mean zonal flow characteristics, averaged over azimuth and time. **(a)** Zonal flow profiles on the outer shell boundary as a function of latitude in Rossby number units, $Ro_{ZF} = \overline{U_\phi}/(\Omega r_o)$. Color denotes Pm. **(b)** Zonal flows (Ro_{ZF}) and meridional circulation patterns for the (left) $Pm = 5$, (middle) $Pm = 1$, and (right) $Pm = 0.25$ cases. Red (blue) indicates the prograde (retrograde) flow direction, while solid (dashed) black contours denote clockwise (counterclockwise) circulations. **(c)** Equatorial zonal flow velocity (α_e) from **(a)** plotted versus the local magnetic Rossby number. Vertical magenta lines demarcate approximate regime boundaries.

4.3 Magnetic Fields

Magnetic field morphology is quantified in Figure 6 based on the behavior of the magnetic power spectra of the fluid shell up to spherical harmonic degree (n) and order (m) 20. The spectra demonstrate that models with $Pm \geq 2$, or $Ro_{M,\ell} \lesssim 1$, are characterized by small-scale, strongly multipolar dynamos with significant power over a broad range of spherical harmonic degrees (panel a). For these models, the axisymmetric ($m = 0$) contribution is distinctly small compared to the $m = 1$ peak that is followed by a gradual decay towards smaller scales with higher m values (panel b). Conversely, models with $Pm \leq 0.5$, or $Ro_{M,\ell} \gtrsim 7$, are characterized by a substantial quadrupole ($n = 2$) component (panel e) and have peak power in the axisymmetric $m = 0$ mode (panel f). The intermediate $Pm = [0.75, 1.0]$ models ($3.5 \lesssim Ro_{M,\ell} \lesssim 6.4$) show combinations of these behaviors (panels c and d). The $Pm = 1$ case (shown in pink) has a relatively flat spectra as a function of n with the highest amplitude (marginally) at $n = 2$ and a prominent peak at $m = 1$, while the $Pm = 0.75$ case (shown in red) has a more substantial peak at $n = 2$ and a less substantial peak at $m = 1$.

Figure 6 insets also show radial magnetic fields at the outer boundary in each magnetic regime. These random snapshots in time are plotted at full spatial resolution (i.e. up to $n = n_{max}$) and further illustrate that the radial magnetic field becomes larger scale and weaker as the magnetic Prandtl number decreases, or equivalently, as the local magnetic Rossby number decreases.

The characteristic length scale for the magnetic field is defined as

$$\ell_B/D = \pi/(2\overline{k_B}), \quad \text{where} \quad \overline{k_B} = \sqrt{\overline{n_B}^2 + \overline{m_B}^2} \tag{17}$$

with

$$\overline{n_B} = \sum_{n=1}^{n_{max}} \frac{n\langle \mathbf{B}_n \cdot \mathbf{B}_n \rangle}{\langle \mathbf{B} \cdot \mathbf{B} \rangle} \quad \text{and} \quad \overline{m_B} = \sum_{m=0}^{m_{max}} \frac{m\langle \mathbf{B}_m \cdot \mathbf{B}_m \rangle}{\langle \mathbf{B} \cdot \mathbf{B} \rangle}. \tag{18}$$

following Christensen & Aubert (2006) and Soderlund et al. (2012), among others. The smallest length scales occur in cases with the strongest magnetic fields, while the weakest field case exhibits the largest scales — differing by nearly a factor of four (Table 3). For all models, the magnetic length scale is substantially smaller than the

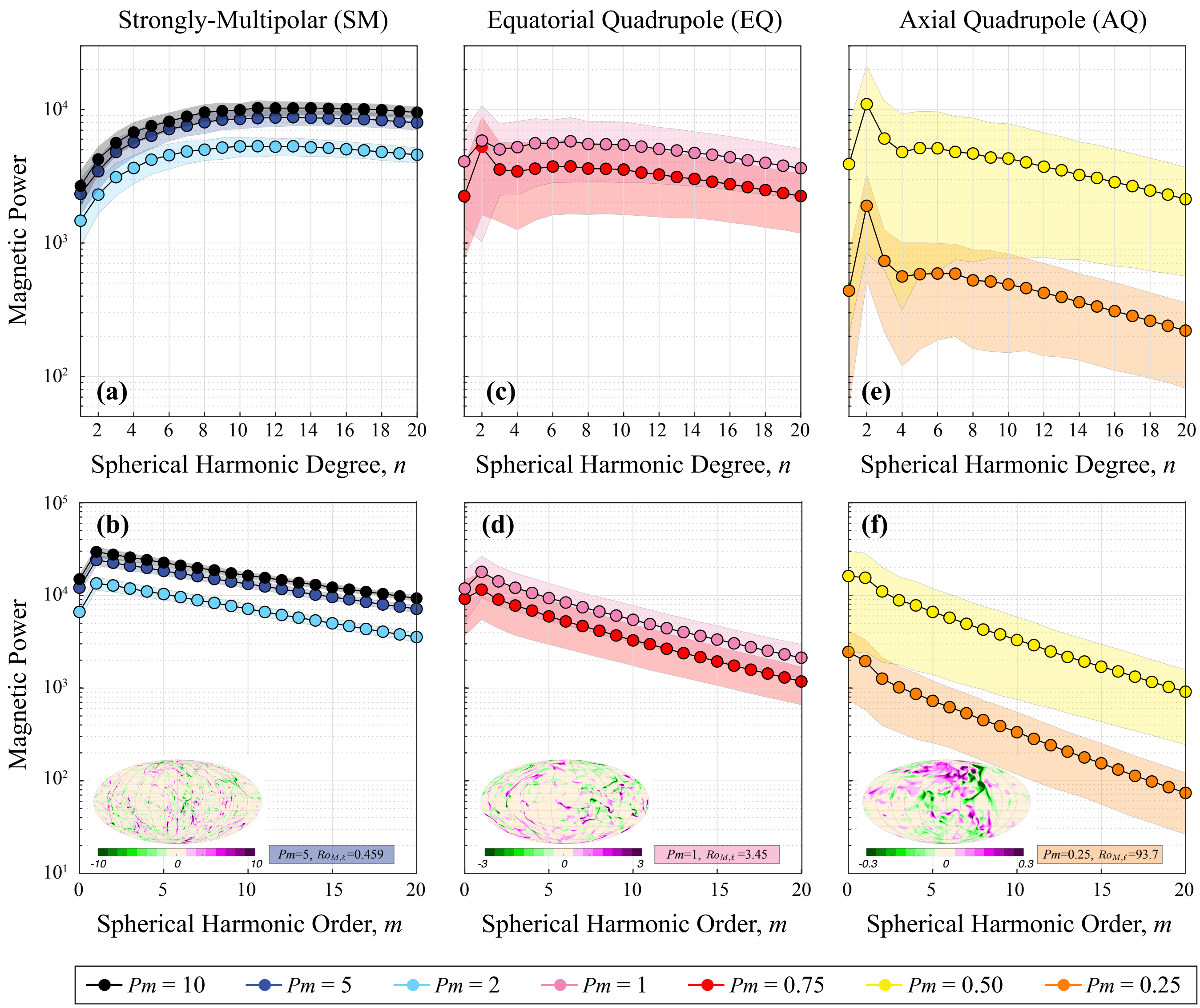

Figure 6. Volumetric magnetic power spectra as a function of spherical harmonic degree n (top row) and order m (bottom row). Left column: models in the S-MS regime; middle column: models in the AS-EQ regime; right column: models in the AS-AQ regime. Markers denote the rms values, while colored envelopes denote the standard deviation. In all panels, color denotes Pm. Embedded within the lower panels are random snapshots of the radial magnetic field on the outer boundary, where field intensity is in non-dimensional $\sqrt{\Lambda}$ units and purple (green) denotes outward (inward) directed field.

velocity length scale, with ℓ_U/ℓ_B being slightly larger than 10 in the intermediate AS-EQ regime and slightly smaller than 10 otherwise.

The local magnetic Rossby number can be expressed as the ratio of kinetic to magnetic energies times the ratio of magnetic to kinetic length scales, as defined in equation (7). Across our survey, the kinetic energy density is larger than the magnetic energy density by at least a factor of two and up to 500 in the lowest Pm case (Table 3). In combination with the non-unity ℓ_B/ℓ_U length scale ratio (Table 3), this explains the factor of 300 change in local magnetic Rossby number across the survey, which contrasts with the fixed $Ro_C = 1.4$ convective Rossby number. This suggests that a triple balance between buoyancy, Coriolis, and Lorentz must be considered for cases in which both Ro_C and $Ro_{M,\ell}$ are of order unity.

4.4 Force Calculations

We have argued that the local magnetic Rossby number approximates the ratio of buoyant inertia to Lorentz forces in dynamo systems. Toward testing this hypothesis, we calculate volumetric integrals of each term in the momentum equation (9):

$$F = \int_V \left(\mathcal{F}_r^2 + \mathcal{F}_\theta^2 + \mathcal{F}_\phi^2\right)^{1/2} dV, \tag{19}$$

where $\mathcal{F}$ is a generic force density (e.g., Soderlund et al. 2012) and V is the volume of the spherical shell. Figure 7 shows timeseries of the force integrals for representative cases of each regime. The $Pm = 5$ case is in the so-called magnetostatic regime in which pressure (F_P) balances the Lorentz force (F_L) at leading order (e.g., Roberts 1967). The advective inertia (F_I) and Coriolis (F_C) terms are comparable, as are the diffusive (F_D) and flow changes (F_U) contributions. The buoyancy term (F_B) is weakest in this S-SM regime. The $Pm = 1$ and

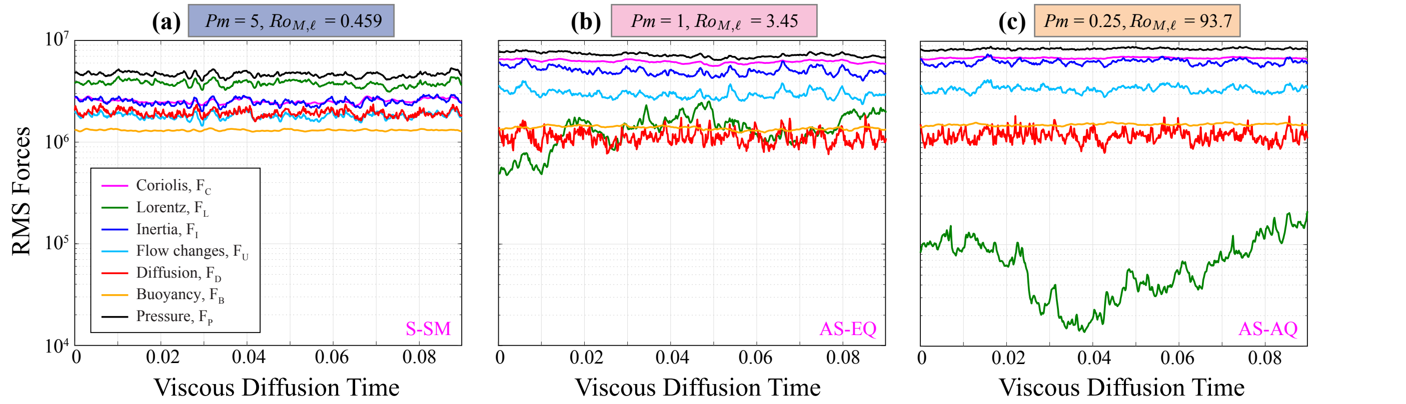

Figure 7. Time series over a representative period of the volume-averaged root-mean-square force integrals for each term of the momentum equation for the **(a)** $Pm = 5$, **(b)** $Pm = 1$, and **(c)** $Pm = 0.25$ cases.

$Pm = 0.25$ cases, in contrast, have a leading order balance between pressure and Coriolis forces with advection playing a significant role and flow changes secondarily. The largest difference between these two cases is the relative strength of the Lorentz term: it is comparable to buoyancy and diffusion in the $Pm = 1$ case and approximately an order of magnitude weaker in the $Pm = 0.25$. The subdominance of the Lorentz force in these AS-EQ and AS-AQ cases is consistent with their DR behavior following the non-magnetic results. Future work will focus on the mechanisms responsible for the solar-like differential rotation.

With these timeseries, we are able to calculate the ratio of inertia to Lorentz forces directly. We find $\langle F_I \rangle / \langle F_L \rangle = 0.662$ for $Pm = 5$, compared to $Ro_{M,\ell} = 0.459$. For $Pm = 1$, $\langle F_I \rangle / \langle F_L \rangle = 3.68$ compared to $Ro_{M,\ell} = 3.45$. For $Pm = 0.25$, $\langle F_I \rangle / \langle F_L \rangle = 87.8$ compared to $Ro_{M,\ell} = 93.7$. Expanding to consider all of our models as well as available data in the literature, Figure 8 plots the inertia / Lorentz force ratios against the local magnetic Rossby number. This comparison indicates good agreement between the two quantities across nearly four orders of magnitude, diverging only slightly when their values are less than unity. We thus conclude that $Ro_{M,\ell}$ is a good proxy for the ratio of inertial to Lorentz forces.

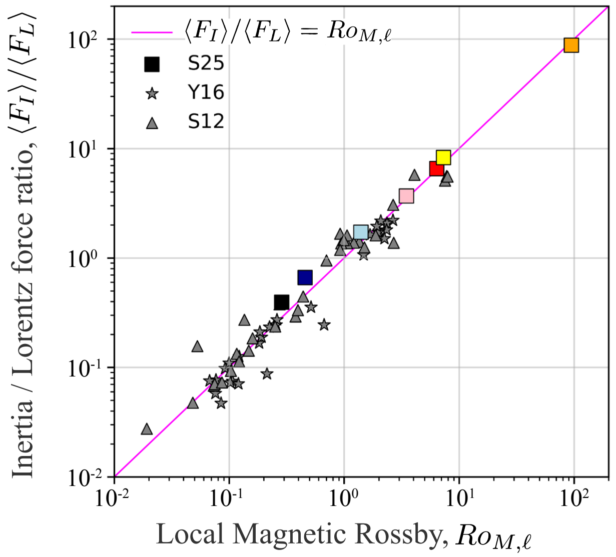

Figure 8. The ratio of inertia to Lorentz forces, $\langle F_I \rangle / \langle F_L \rangle$, plotted as a function of the local magnetic Rossby number, $Ro_{M,\ell}$. The diagonal magenta line demarcates equivalence of the two quantities. Marker shape indicates the source publication, while internal marker color for the models in this study (S25) denotes Pm as in other figure panels. S25 and Soderlund et al. (2012) (S12) include boundary layers in the volume integration, which are excluded in Yadav et al. (2016a) (Y16).

5 DISCUSSION AND CONCLUSIONS

Here we have carried out a selected set of Boussinesq dynamo models in which we vary the value of the magnetic Prandtl number such that the intensity of the dynamo field varies between different cases, all made at fixed $Pr = 1$ and $Ro_C = 1.4$. We purposely set Ro_C near unity, the hydrodynamical differential rotation transition point, in hopes of controlling the differential rotation transition by means of the Lorentz force.

A sharp transition in differential rotation was found in the vicinity of $Ro_{M,\ell} \sim 1$ in our models, accompanied by more gradual changes in dynamo morphology. Thus, our simulations support the hypothesis that magnetic forces are a significant factor in the location of the behavioral transitions in turbulent MHD systems. Alternatively stated, it has been found that Ro_ℓ controls transitions in studies in which it is the broadly varied parameter (e.g., Gilman 1978; Aurnou et al. 2007; Gastine et al. 2013; Guerrero et al. 2013; Käpylä et al. 2014; Mabuchi et al. 2015; Camisassa & Featherstone 2022), whereas $Ro_{M,\ell}$ is the transition parameter found here when it is the parameter that is broadly varied (also see, e.g., Fan & Fang 2014; Hotta et al. 2022; Menu et al. 2020; Zaire et al. 2022; Käpylä 2023).

Our findings imply that the behavioral transitions in stellar convection zone dynamics are governed partially by a local-scale triple balance between inertia, Coriolis, and Lorentz forces. This idea is not new. For instance, Calkins et al. (2015) derived a set of quasi-geostrophic dynamo equations in which the local-scale balance exists between the buoyant inertial, Coriolis, and Lorentz terms. This predicted local-scale triple balance has since been found to exist in a number of analyses of planetary dynamo simulations (e.g., Yadav et al. 2016a; Dormy 2016; Aurnou & King 2017; Aubert 2020; Schwaiger et al. 2021; Nakagawa & Davies 2022).

Figure 9 further elucidates how convection zone regime transitions may be controlled by a buoyant inertial, Coriolis, and Lorentz triple balance. Here, the dipolarity f_D from an ensemble of stellar

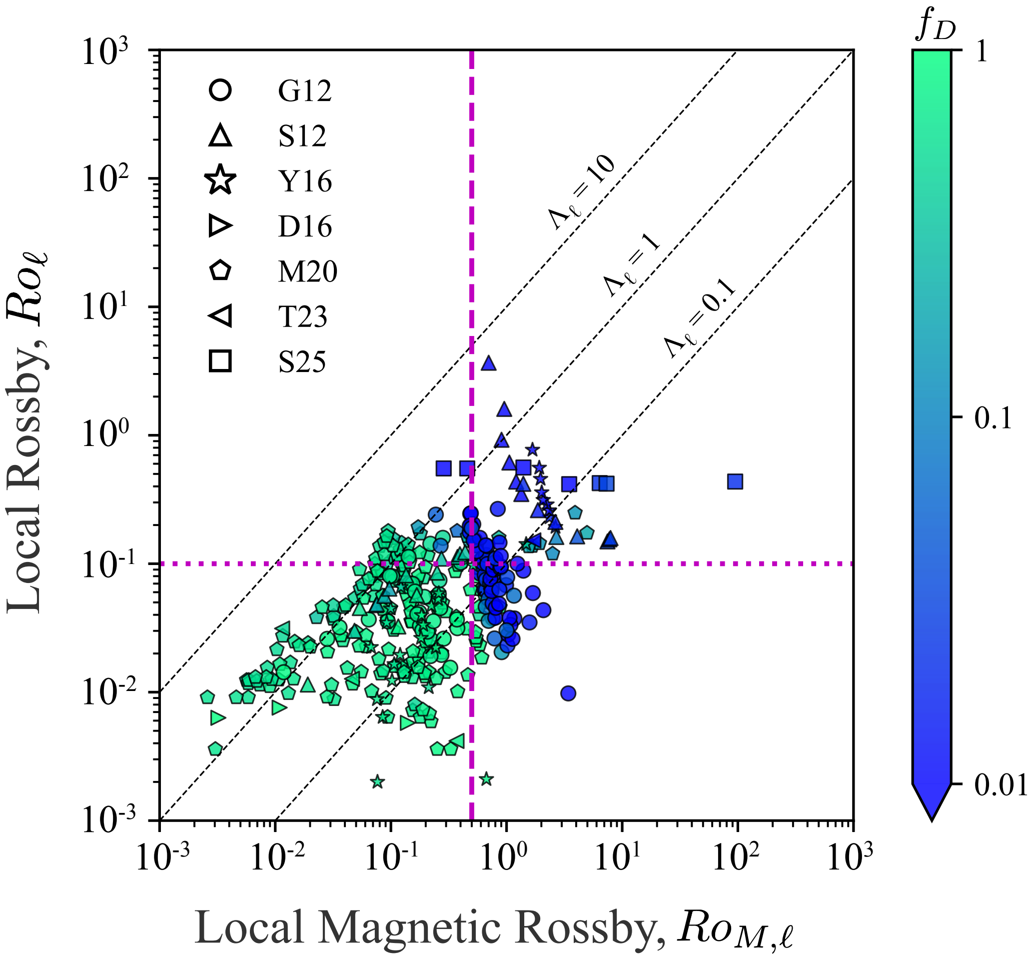

Figure 9. Regime diagram showing dipolarity, f_D, in color as a function of the local Rossby number, Ro_ℓ, and the local magnetic Rossby number, $Ro_{M,\ell}$. The purple lines indicate hypothesized transitions between dipole-dominated (green) and multipolar dynamos (blue): the vertical dashed line indicates $Ro_{M,\ell} = 0.5$ and the horizontal dotted line indicates $Ro_\ell = 0.1$. The thin dashed black lines denote constant Λ_ℓ values. Sources: Gastine et al. (2012) (G12), Soderlund et al. (2012) (S12), Dormy (2016) (D16), Menu et al. (2020) (M20), Teed & Dormy (2023) (T23), and this study (S25).

and planetary dynamo modeling studies is plotted as a function of $Ro_{M,\ell}$ on the abscissa and Ro_ℓ on the ordinate. Symbol shapes indicate the study from which the data were collected, while the symbol fill color represents the f_D value, with a logarithmic scale transitioning from blue to green. The log color scaling pivots around $f_D \approx 0.1$. Dipolar B-field cases with $f_D \gtrsim 0.1$ have green fill colors; multipolar cases with $f_D \lesssim 0.1$ have blue fill. We believe this gives a sensible log-scale dipolarity cut-off given that f_D varies by nearly six orders of magnitude in Figure 3.

The two purple lines in Figure 9 mark the estimated transition locations based on dipolarity data in Figure 3. The horizontal dotted purple line marks the postulated $Ro_\ell \simeq 0.1$ transition (e.g., Christensen 2006, cf. Figure 3c), while the vertical dashed purple line marks the estimated $Ro_{M,\ell} \simeq 0.5$ dipolarity transition in Figure 3d. In addition, the thin black dashed diagonals in Figure 9 correspond to constant values of Λ_ℓ since, following equation (8), the local Elsasser number is defined as $\Lambda_\ell = Ro_\ell / Ro_{M,\ell}$.

The data compilation in Figure 9 comes from a broad array of spherical shell dynamo modeling studies, both stellar and planetary, anelastic and Boussinesq, and over a range of Pr, Pm, E, and thermo-mechanical boundary conditions. Despite the broad range of sources, robust trends exist in the f_D data, defining different behavioral regimes of dynamo generation in this (Ro_ℓ^M, Ro_ℓ) parameter space. First, dipolar cases ($f_D \gtrsim 0.1$) exist primarily below $Ro_\ell = 0.2$ and $Ro_{M,\ell} = 0.5$.

The dipolar cases are not evenly spread across the ($Ro_{M,\ell} < 0.5$, $Ro_\ell < 0.2$) quadrant of Figure 9. Instead, they are bounded by the $\Lambda_\ell \approx 3$ diagonal line from above. Thus, the dipolar cases occupy a wedge-like region bounded by ($Ro_{M,\ell} \lesssim 0.5$, $\Lambda_\ell \lesssim 3$). An implication of this dipolar wedge is that the hydrodynamic $Ro_\ell \sim 0.1$ transition in dynamo morphology proposed in Christensen & Aubert (2006) may hold only locally in the vicinity of $0.05 \lesssim Ro_{M,\ell} \lesssim 0.5$ in Figure 9, roughly where the $\Lambda_\ell \sim 1$ and $Ro_{M,\ell} \sim 0.5$ lines intersect. The general validity of the hydrodynamic $Ro_\ell \approx 0.1$ transition argument is put into question by the sharp change in f_D at $Ro_{M,\ell} \gtrsim 0.5$. Furthermore, if future dynamo cases in the $Ro_\ell \lesssim 0.1$ and $\Lambda_\ell \gtrsim 3$ region of parameter space are found to be non-dipolar, then the $Ro_\ell \approx 0.1$ dynamo transition will need to be fundamentally reconsidered — likely in favor of an MHD-based explanation that better fits the data.

The fixed $Ro_C = 1.4$ data from this study are demarcated by square symbols in Figure 9. With Ro_ℓ values ranging from 0.4 to 0.6, our cases all lie above the dipolar wedge and, indeed, all have non-dipolar magnetic fields. Yet changes in magnetic field morphology

(Table 4) and differential rotation pattern (Figure 5) still occur in our cases, occurring over $Ro_{M,\ell} \approx 1$ to 7. This leads us to hypothesize that $Ro_{M,\ell} = O(1)$ may control the behavior of convection zone transitions over a wide range of Ro_ℓ values, possibly including $Ro_\ell \gg 1$.

The dipolar wedge's $\Lambda_\ell \approx 3$ bounding line in Figure 9 suggests that dipolar dynamo simulations are attracted to convection-scale dynamics that are in local magnetostrophic balance with $\Lambda_\ell \sim 1$ (e.g., Calkins et al. 2015; King & Aurnou 2015; Soderlund et al. 2015; Dormy 2016; Aurnou & King 2017; Menu et al. 2020; Hotta et al. 2022). The $Ro_{M,\ell} \approx 0.5$ upper bound on the wedge implies that dipolar solutions are stable until inertial accelerations become comparable to the Lorentz terms, in good agreement with the force balance calculations of Yadav et al. (2016a) and following studies. Thus, the wedge suggests that dipolar dynamo action in current-day simulations exists in a triple balance where local-scale Coriolis forces may be approached by Lorentz forces from below, which may be approached by inertial forces, also from below.

Careful inspection of Figure 9 suggests that the separation between the dipolar and multipolar dynamo morphology cases occurs along a line that is slightly off-vertical. Determining the robustness of this tilted transition line and elucidating the physics that sets its slope are open topics. Further, the behavior of dynamos in the high-Ro_ℓ, high-$Ro_{M,\ell}$ region of parameter space remains largely uninvestigated as well. It remains also to be shown how best to replace the *a posteriori* local Rossby numbers with *a priori* control parameters. A version of Figure 9 made with pure input parameters on both axes will lead to far more predictive power and more meaningful testing of regime transition hypotheses.

Figure 9 should ideally include a second panel highlighting transitions in differential rotation, based on an ensemble of α_e as a function of $Ro_{M,\ell}$ and Ro_ℓ values from spherical shell dynamo simulations. To our consternation, a comparable plot of α_e as a function of $Ro_{M,\ell}$ and Ro_ℓ remains to be made, since we were unable to assemble an α_e dataset from the existing literature. Thus, we must for now leave unanswered whether or not broadly similar regime boundaries as those found in Figure 9 also exist for transitions between solar and anti-solar differential rotation.

ACKNOWLEDGEMENTS

The authors thank L. Matilsky for an in-depth, comprehensive review that significantly improved the paper; T. Schwaiger, M. Calkins, and C. Yan for helpful insights, and E. Dormy, T. Gastine, R. Teed, B. Zaire, and R. Yadav for providing datasets and discussions. The authors thank the Isaac Newton Institute for Mathematical Sciences, Cambridge, UK, for support and hospitality during the programme "Dynamos in planets and stars - similarities and differences," supported by EPSRC grant EP/R014604/1, where work on this paper was undertaken. KMS acknowledges support from the National Science Foundation (NSF) Astronomy and Astrophysics program via award AST #2308185. PNW acknowledges support from the NASA Juno project and NASA CDAP grant No. 80NSSC23K0511. PJK acknowledges support by the Deutsche Forschungsgemeinschaft (DFG, German Research Foundation) Heisenberg programme (grant No. KA 4825/4-1), and by the Munich Institute for Astro-, Particle and BioPhysics (MIAPbP) funded by the DFG under Germany's Excellence Strategy – EXC-2094 – 390783311. JMA thanks the NSF Geophysics Program for support via award EAR #2143939. Computing resources supporting this work were provided by the NASA High-End Computing (HEC) Program through the NASA Advanced Supercomputing (NAS) Division at Ames Research Center. We have no conflicts of interest to disclose.

DATA AVAILABILITY

We use the dynamo code MagIC (Wicht 2002; Gastine & Wicht 2012) with the SHTns library to efficiently calculate the spherical harmonic transforms (Schaeffer 2013); the open source code is available at https://github.com/magic-sph/magic. Model results are tabulated in the manuscript.

REFERENCES

Aubert J., 2020, Geophysical Journal International, 221, 378
Aurnou J., King E., 2017, Proceedings of the Royal Society A: Mathematical, Physical and Engineering Sciences, 473, 20160731
Aurnou J. M., Andreadis S., Zhu L., Olson P. L., 2003, Earth Planet. Sci. Lett., 212, 119
Aurnou J. M., Heimpel M. H., Wicht J., 2007, Icarus, 190, 110
Aurnou J. M., Heimpel M. H., Allen L., King E. M., Wicht J., 2008, Geophys. J. Int., 173, 793
Aurnou J. M., Horn S., Julien K., 2020, Physical Review Research, 2, 043115
Balbus S. A., 2009, Monthly Notices of the Royal Astronomical Society, 395, 2056
Barik A., Triana S., Calkins M., Stanley S., Aurnou J., 2023, Earth and Space Science, 10, e2022EA002606
Brun A. S., Palacios A., 2009, Astrophys. J., 702, 1078
Brun A. S., Strugarek A., Noraz Q., Perri B., Varela J., Augustson K., Charbonneau P., Toomre J., 2022, The Astrophysical Journal, 926, 21
Calkins M. A., Julien K., Tobias S. M., Aurnou J. M., 2015, J. Fluid Mech., 780, 143
Camisassa M. E., Featherstone N. A., 2022, The Astrophysical Journal, 938, 65
Cardin P., Brito D., Jault D., Nataf H. C., Masson J. P., 2002, Magnetohydrodynamics, 38, 177
Christensen U. R., 2006, Nature, 444, 1056
Christensen U. R., 2010, Space Sci. Rev., 152, 565
Christensen U. R., Aubert J., 2006, Geophys. J. Int., 166, 97
Davidson P. A., 2001, An introduction to magnetohydrodynamics. Cambridge: Cambridge University Press
Dormy E., 2016, Journal of Fluid Mechanics, 789, 500
Dormy E., 2025, Annual Review of Fluid Mechanics, 57
Elliott J., Miesch M., Toomre J., 2000, The Astrophysical Journal, 533, 546
Fan Y., Fang F., 2014, The Astrophysical Journal, 789, 35
Featherstone N. A., Hindman B. W., 2016, The Astrophysical Journal Letters, 830, L15
Featherstone N. A., Miesch M. S., 2015, Astrophys. J., 804, 67
Garaud P., 2021, Physical Review Fluids, 6, 030501
Gastine T., Aurnou J. M., 2023, Journal of Fluid Mechanics, 954, R1
Gastine T., Wicht J., 2012, Icarus, 219, 428
Gastine T., Duarte L., Wicht J., 2012, Astron. Astrophys., 546, A19
Gastine T., Wicht J., Aurnou J. M., 2013, Icarus, 225, 156
Gastine T., Heimpel M., Wicht J., 2014a, Physics of the Earth and Planetary Interiors, 232, 36
Gastine T., Yadav R. K., Morin J., Reiners A., Wicht J., 2014b, MNRAS, 438, L76
Gilman P. A., 1977, Geophys. Astrophys. Fluid Dyn., 8, 93
Gilman P. A., 1978, Geophys. Astrophys. Fluid Dyn., 11, 157
Gilman P. A., Foukal P. V., 1979, Astrophys. J., 229, 1179
Glatzmaier G. A., Gilman P. A., 1981, Astrophys. J. Supp., 45, 381
Glazier J., Segawa T., Naert A., Sano M., 1999, Nature, 393, 307
Grannan A. M., Cheng J. S., Aggarwal A., Hawkins E. K., Xu Y., Horn S., Sánchez-Álvarez J., Aurnou J. M., 2022, Journal of Fluid Mechanics, 939, R1

Guerrero G., Smolarkiewicz P., Kosovichev A., Mansour N., 2013, The Astrophysical Journal, 779, 176
Guervilly C., Cardin P., Schaeffer N., 2019, Nature, 570, 368
Guilet J., Reboul-Salze A., Raynaud R., Bugli M., Gallet B., 2022, Monthly Notices of the Royal Astronomical Society, 516, 4346
Guseva A., Petitdemange L., Pinçon C., 2025, arXiv preprint arXiv:2505.06618
Hadjerci G., Bouillaut V., Miquel B., Gallet B., 2024, arXiv preprint arXiv:2401.16200
Hindman B. W., Featherstone N. A., Julien K., 2020, The Astrophysical Journal, 898, 120
Horn S., Aurnou J. M., 2022, Proceedings of the Royal Society A, 478, 20220313
Horn S., Aurnou J. M., 2024, Royal Society of London. Proceedings A. Mathematical, Physical and Engineering Sciences, pp In–Press
Hotta H., Iida Y., Yokoyama T., 2012, The Astrophysical Journal Letters, 751, L9
Hotta H., Rempel M., Yokoyama T., 2015, ApJ, 798, 51
Hotta H., Kusano K., Shimada R., 2022, The Astrophysical Journal, 933, 199
Julien K., Knobloch E., 2007, Journal of Mathematical physics, 48
Käpylä P. J., 2023, Astronomy & Astrophysics, 669, A98
Käpylä P. J., Singh N. K., 2022, Journal of Fluid Mechanics, 952, R1
Käpylä P. J., Mantere M. J., Brandenburg A., 2011, Astron. Nachr., 332, 883
Käpylä P. J., Mantere M. J., Cole E., Warnecke J., Brandenburg A., 2013, ApJ, 778, 41
Käpylä P. J., Käpylä M. J., Brandenburg A., 2014, Astron. Astrophys., 570, A43
Käpylä P. J., Gent F. A., Olspert N., Käpylä M. J., Brandenburg A., 2020, Geophysical and Astrophysical Fluid Dynamics, 114, 8
Käpylä P. J., Browning M. K., Brun A. S., Guerrero G., Warnecke J., 2023, Space Science Reviews, 219, 58
Karak B. B., Käpylä P. J., Käpylä M. J., Brandenburg A., Olspert N., Pelt J., 2015, Astronomy & Astrophysics, 576, A26
King E. M., Aurnou J. M., 2013, Proc. Natl. Acad. Sci., 110, 6688
King E. M., Aurnou J. M., 2015, Proc. Natl. Acad. Sci., 112, 990
King E. M., Stellmach S., Noir J., Hansen U., Aurnou J. M., 2009, Nature, 457, 301
Lehtinen J. J., Käpylä M. J., Olspert N., Spada F., 2021, The Astrophysical Journal, 910, 110
Lemasquerier D. G., Bierson C. J., Soderlund K. M., 2023, AGU Advances, 4, e2023AV000994
Mabuchi J., Masada Y., Kageyama A., 2015, Astrophys. J., 806, 10
Matilsky L. I., Hindman B. W., Toomre J., 2019, The Astrophysical Journal, 871, 217
Matilsky L. I., Hindman B. W., Toomre J., 2020, The Astrophysical Journal, 898, 111
Matilsky L. I., Brummell N. H., Hindman B. W., Toomre J., 2024, The Astrophysical Journal, 962, 189
Menu M. D., Petitdemange L., Galtier S., 2020, Physics of the Earth and Planetary Interiors, 307, 106542
Metcalfe T. S., Egeland R., van Saders J., 2016, ApJ, 826, L2
Miesch M. S., Toomre J., 2009, Annu. Rev. Fluid Mech., 41, 317
Nakagawa T., Davies C. J., 2022, Earth and Planetary Science Letters, 594, 117752
Nath D., Pandey A., Kumar A., Verma M., 2016, Phys. Rev. Fluids, 1, 064302
Oliver T. G., Jacobi A. S., Julien K., Calkins M. A., 2023, Physical Review Fluids, 8, 093502
Pandey A., Krasnov D., Schumacher J., Samtaney R., Sreenivasan K. R., 2022, Physica D Nonlinear Phenomena, 442, 133537
Plumley M., Julien K., 2019, Earth and Space Science, 6, 1580
Ponty Y., Mininni P., Montgomery D., Pinton J.-F., Politano H., Pouquet A., 2005, Physical Review Letters, 94, 164502
Reinhold T., Arlt R., 2015, Astronomy & Astrophysics, 576, A15
Roberts P., 1967, An introduction to magnetohydrodynamics. Vol. 6, Longmans London
Roberts P. H., Aurnou J. M., 2012, Geophysical & Astrophysical Fluid Dynamics, 106, 157
Roberts P. H., King E. M., 2013, Rep. Prog. Phys., 76, 096801
Sarris I., Zikos G., Grecos A., Vlachos N., 2006, Numerical Heat Transfer, Part B: Fundamentals, 50, 157
Schaeffer N., 2013, Geochemistry, Geophysics, Geosystems, 14, 751
Schaeffer N., Jault D., Cardin P., Drouard M., 2012, Geophysical Journal International, 191, 508
Schaeffer N., Jault D., Nataf H.-C., Fournier A., 2017, Geophys. J. Int., 211, 1
Schekochihin A. A., Cowley S. C., Maron J. L., McWilliams J. C., 2004, Physical review letters, 92, 054502
Schwaiger T., Gastine T., Aubert J., 2021, Geophysical Journal International, 224, 1890
Soderlund K. M., 2019, Geophys. Res. Lett., 46, 8700
Soderlund K. M., King E. M., Aurnou J. M., 2012, Earth Planet. Sci. Lett., 333-334, 9
Soderlund K. M., Heimpel M. H., King E. M., Aurnou J. M., 2013, Icarus, 224, 97
Soderlund K. M., Schmidt B. E., Wicht J., Blankenship D. D., 2014, Nature Geosci., 7, 16
Soderlund K. M., Sheyko A., King E. M., Aurnou J. M., 2015, Prog. Earth Planet. Sci., 2, 24
Sommeria J., Moreau R., 1982, Journal of Fluid Mechanics, 118, 507
Spiegel E. A., 1971, Annu. Rev. Earth Planet. Sci., 9, 323
Stellmach S., Lischper M., Julien K., Vasil G. M., Cheng J. S., Ribeiro A., King E. M., Aurnou J. M., 2014, Phys. Rev. Lett., 113, 254501
Teed R. J., Dormy E., 2023, Journal of Fluid Mechanics, 964, A26
Tikoo S. M., Evans A. J., 2022, Annual Review of Earth and Planetary Sciences, 50, 99
Vasil G. M., Julien K., Featherstone N. A., 2021, Proceedings of the National Academy of Sciences, 118, e2022518118
Viviani M., Warnecke J., Käpylä M. J., Käpylä P. J., Olspert N., Cole-Kodikara E. M., Lehtinen J. J., Brandenburg A., 2018, Astronomy & Astrophysics, 616, A160
Viviani M., Käpylä M. J., Warnecke J., Käpylä P., Rheinhardt M., 2019, The Astrophysical Journal, 886, 21
Wicht J., 2002, Phys. Earth Planet. Int., 132, 281
Xu Y., Horn S., Aurnou J. M., 2023, Physical Review Fluids, 8, 103503
Yadav R. K., Gastine T., Christensen U. R., Wolk S. J., Poppenhaeger K., 2016a, Proceedings of the National Academy of Sciences, 113, 12065
Yadav R. K., Gastine T., Christensen U. R., Duarte L. D., Reiners A., 2016b, Geophysical Journal International, 204, 1120
Yan M., Calkins M. A., Maffei S., Julien K., Tobias S. M., Marti P., 2019, Journal of Fluid Mechanics, 877, 1186
Zaire B., Jouve L., Gastine T., Donati J., Morin J., Landin N., Folsom C., 2022, Monthly Notices of the Royal Astronomical Society, 517, 3392

This paper has been typeset from a TEX/LATEX file prepared by the author.